Artificial intelligence-enabled automated analysis of transmission electron micrographs to evaluate chemotherapy impact on mitochondrial morphology in triple negative breast cancer

Argenis Arriojas[1,*], Lily M. Baek[2,*], Mariah J. Berner[2], Alexander Zhurkevich[3], Antentor Othrell Hinton Jr.[4,5], Matthew D. Meyer[6], Lacey E. Dobrolecki[2], Michael T. Lewis[2,7,9], Kourosh Zarringhalam[1,10,#], Gloria V. Echeverria[2,7-9,#]

[1] Center for Personalized Cancer Therapies, University of Massachusetts Boston, Boston, MA, USA

[2] Lester and Sue Smith Breast Center and Department of Medicine, Baylor College of Medicine, Houston, TX, USA

[3] Department of Computer Science, University of Massachusetts Boston, Boston, MA, USA

[4] Department of Molecular Physiology and Biophysics, Vanderbilt University, Nashville, TN, USA

[5] Microscopy and Cell Analysis Core Facility, Mayo Clinic, Rochester, MN, USA

[6] Shared Equipment Authority, Rice University, Houston, TX, USA

[7] Dan L Duncan Comprehensive Cancer Center, Baylor College of Medicine. Houston, TX, USA

[8] Department of Medicine, Baylor College of Medicine, Houston, TX, USA.

[9] Departments of Molecular and Cellular Biology and Radiology. Baylor College of Medicine. Houston, TX, USA

[10] Department of Mathematics, University of Massachusetts Boston, Boston, MA, USA

* These authors contributed equally to this work

[#] co-corresponding authors

DISCLOSURES

MTL is a founder and limited partner in StemMed Ltd. and a manager in StemMed Holdings, its general partner. He is a founder and equity stakeholder in Tvardi Therapeutics Inc. Some PDXs are exclusively licensed to StemMed Ltd., resulting in royalty income to MTL. LED is a compensated employee of StemMed Ltd. Some PDXs are exclusively licensed to StemMed Ltd. resulting in royalty income to LED. G.V.E. receives sponsored research funding from Chimerix, Inc. G.V.E. receives experimental compounds from the Lead Discovery Center of Germany. All other authors have nothing to disclose.

ABSTRACT

Advancements in transmission electron microscopy (TEM) have enabled in-depth studies of biological specimens, offering new avenues to large-scale imaging experiments with subcellular resolution. Mitochondrial structure is of growing interest in cancer biology due to its crucial role in regulating the multi-faceted functions of mitochondria. We and others have established the crucial role of mitochondria in triple-negative breast cancer (TNBC), an aggressive subtype of breast cancer with limited therapeutic options. Building upon our previous work demonstrating the regulatory role of mitochondrial structure dynamics in metabolic adaptation and survival of chemotherapy-refractory TNBC cells, we sought to extend those findings to a large-scale analysis of transmission electron micrographs. Here we present a UNet artificial intelligence (AI) model for automatic annotation and assessment of mitochondrial morphology and feature quantification. Our model is trained on 11,039 manually annotated mitochondria across 125 micrographs derived from a variety of orthotopic patient-derived xenograft (PDX) mouse model tumors and adherent cell cultures. The model achieves an F1 score of 0.85 on test micrographs at the pixel level. To validate the ability of our model to detect expected mitochondrial structural features, we utilized micrographs from mouse primary skeletal muscle cells genetically modified to lack Dynamin-related protein 1 (Drp1). The algorithm successfully detected a significant increase in mitochondrial elongation, in alignment with the well-established role of Drp1 as a driver of mitochondrial fission. Further, we subjected *in vitro* and *in vivo* TNBC models to conventional chemotherapy treatments commonly used for clinical management of TNBC, including doxorubicin, carboplatin, paclitaxel, and docetaxel (DTX). We found substantial within-sample heterogeneity of mitochondrial structure in both *in vitro* and *in vivo* TNBC models and observed a consistent reduction in mitochondrial elongation in DTX-treated specimens. We went on to compare mammary tumors and matched lung metastases in a highly metastatic PDX model of TNBC, uncovering significant reduction in mitochondrial length in metastatic lesions. Our large, curated dataset provides high statistical power to detect frequent chemotherapy-induced shifts in mitochondrial shapes and sizes in residual cells left behind after treatment. The successful application of our AI model to capture mitochondrial structure

marks a step forward in high-throughput analysis of mitochondrial structures, enhancing our understanding of how morphological changes may relate to chemotherapy efficacy and mechanism of action. Finally, our large, manually curated electron micrograph dataset - now publicly available - serves as a unique gold-standard resource for developing, benchmarking, and applying computational models, while further advancing investigations into mitochondrial morphology and its impact on cancer biology.

INTRODUCTION

Mitochondria are essential organelles responsible for energy production through oxidative phosphorylation (OXPHOS). This process generates ATP, the cell's primary energy currency, by utilizing electrons derived from nutrients[1]. Beyond energy production, mitochondria play critical roles in regulating various cellular processes, including apoptosis, cell cycle control, and metabolic signaling, all of which are dependent on their structural integrity[2-5].

Mitochondrial structure, regulated by their fusion and fission, is highly dynamic. These organelles are enclosed by a double membrane, with the inner membrane folded into cristae that house the OXPHOS machinery[6]. The balance between mitochondrial fusion and fission, governed by key proteins such as dynamin-related protein 1 (DRP1), optic atrophy 1 (OPA1), and mitofusins (MFNs), is crucial for maintaining mitochondrial function and cellular health[7]. In several diseases including cancer, alterations in mitochondrial structure, including those that favor either elongation or fragmentation, are common, contributing to dynamic metabolic reprogramming that supports tumor growth and survival[8-10]. Alterations in mitochondrial fusion and fission processes can lead to enhanced proliferation, metastasis, and other hallmarks of cancer[9]. Thus, understanding these alterations is critical for gaining a deeper understanding of cancer biology.

Triple-negative breast cancer (TNBC) presents significant treatment challenges due to the absence of estrogen and progesterone receptors and human epidermal growth factor receptor two (HER2) amplification/overexpression[11]. Although neoadjuvant (a.k.a pre-surgical) chemotherapy (NACT) with PD-1 immune checkpoint blockers is the standard treatment, approximately half of patients

do not achieve complete tumor eradication, leading to significantly elevated risk of metastasis and mortality[12-14]. In our previous studies, we found that residual patient-derived xenograft (PDX) tumors which eventually recurred underwent reversible transcriptional and mitochondrial adaptations, with notable increases in OXPHOS-related gene expression and activity relative to treatment-naive tumors[15]. This mitochondrial adaptation was mediated by elevation of the mitochondrial fusion protein OPA1. We also demonstrated that inhibiting OPA1 with the small molecule MYLS22[16] effectively reduced mitochondrial fusion, OXPHOS, and chemoresistance[8]. Targeting proteins like DRP1, OPA1, and MFNs could enhance the efficacy of existing treatments and overcome resistance mechanisms, offering new hope for patients with difficult-to-treat cancers[17-20].

Electron microscopy is the gold standard method to gain subcellular resolution of organelles like the mitochondrion. Due to the complexity of mitochondrial structure, accurately quantifying features in imaging data is crucial for understanding the connection between mitochondrial structure and function. Traditionally, analyzing mitochondrial structures involves manually tracing and counting individual mitochondria in electron micrographs to measure morphological parameters such as length, area, circularity, and linearity. This process becomes challenging when the contrast between mitochondria and other organelles is low. In addition, during the manual inspection of mitochondria, the examiner often considers only a subset of the mitochondria in each image, leading to a loss of information. Individual tumor cells can contain anywhere from a few dozen to several hundred mitochondria, making this manual procedure ineffective for statistically powered high-throughput analysis, as it is extremely time-consuming and may be heavily dependent on examiner bias. These issues can lead to unreliable and inconsistent metrics for quantification, especially considering the extensive intra-tumoral heterogeneity characteristic of most cancers.

In recent years, advancements in Artificial intelligence (AI), particularly deep machine learning, have transformed image analysis across various medical domains[21-23], including those focused on mitochondrial inner and outer membrane structure[24]. Deep learning models, especially convolutional neural networks, have shown significant success in tasks such as tumor classification, cancer subtype

identification, mutation prediction, and treatment outcome prediction using histological images like hematoxylin and eosin (H&E) stained slides[25-27]. These approaches utilize either transfer learning, where pre-trained models are fine-tuned for specific tasks, or full-training strategies that train models from scratch using large, domain-specific datasets. Such innovations have enabled the identification of subtle morphological and molecular patterns within images that were previously undetectable through traditional methods. Similarly, AI-driven approaches have advanced mitochondrial structure studies, enabling precise quantification of mitochondrial dynamics and revealing intricate features like cristae topologies that were difficult to detect. Additionally, pixel-level segmentation of cancer images using autoencoder-based architectures has been adapted for high-resolution segmentation tasks across various image types[28-30]. Among these, UNet architectures[31] have demonstrated particular efficacy in pixel-level cancer image analysis[25-27,32]. These methods offer automated segmentation and detection capabilities, facilitating more accurate, efficient, and unbiased quantification with exceptional statistical power.

In this study, we utilized both *in vitro* (adherent cultures of human TNBC cell lines) and *in vivo* (orthotopic PDX mouse models of TNBC) models, in which we previously delineated mitochondrial features and chemotherapeutic responses[15], to conduct a large-scale assessment of mitochondrial morphology. Building on our studies that demonstrated a link between mitochondrial morphology, OXPHOS, and survival in post-chemotherapy residual TNBC cells[8,15], we sought to develop and validate an AI-based approach capable of high-throughput segmentation and quantitative analysis of mitochondrial structures in TNBC. To this end, we first generated a large set of transmission electron micrographs from our models, then curated a high-quality dataset by manually annotating over 11,039 mitochondria across 125 micrographs from the aforementioned models. These manual annotations served as training data for a UNet image segmentation model, which was then applied to detect mitochondria at scale. Using computer-vision approaches, we systematically characterized multiple mitochondrial morphological features. This extensive analysis allowed us to statistically quantify sometimes subtle mitochondrial structural upon chemotherapy treatment with exceptional statistical

rigor. Here, we describe the extensive training and evaluation of our model, demonstrate its robustness and versatility, and present findings that illuminate how mitochondrial structure adapts during treatment in TNBC.

RESULTS

Diverse training datasets to enable robust mitochondrial segmentation

Using our previously established methods to examine residual cells surviving exposure to conventional chemotherapies with *in vivo* and *in vitro* models of TNBC, we systematically collected cell and tumor specimens and subjected them to TEM. We then assembled a diverse training dataset by manually annotating mitochondria from 125 electron micrographs using QuPath[33]. These images ranged in resolution from 43 to 2775 pixel/µm and were collected from two cell culture models – primary mouse skeletal myotubes genetically engineered to lack the mitochondrial fission-driving gene *Drp1* (*Drp1* KO) and human TNBC cells (MDA-MB-231) - as well as seven orthotopic patient-derived xenograft (PDX) TNBC models (PIM001-P, PIM005[15], PIM056[34], WHIM-14[35], BCM-2147[36], BCM-15116 (unpublished), and HCI-010[35]), each derived from a unique TNBC patient. Data acquisition involved three separate microscopists, each employing unique microscope settings and capturing various specimens, including both *in vitro* cell cultures and *in vivo* tumor samples. This diversity in magnification levels, microscope configurations, image formats (including presence of scale bars), and biological systems, ensures that the model learns to recognize mitochondrial structures under varied conditions. This adaptability is critical for its intended application, as it allows for accurate predictions irrespective of resolution or experimental setup.

Model development overview

Figure 1 shows a schematic of our AI pipeline. Briefly, our pipeline began with the preparation of training data, consisting of manually annotated micrographs (Fig.1 and Table 1), following tiling at a common resolution (0.0075 µm/pixel), and data augmentation to enhance model robustness. A U-Net was trained, allowing the model to learn complex features associated with mitochondrial morphology.

The trained model was then utilized to make predictions on new images, detecting and outlining mitochondrial structures. Finally, we performed downstream analyses in two major steps: (1) computer vision tasks (e.g., contour detection, feature characterization such as maximum Feret's diameter and area) and (2) statistical assessments (*e.g.*, distribution measurements and causal analysis) to compare control versus experimental conditions. This streamlined workflow laid the foundation for high-throughput, quantitative evaluation of mitochondrial morphology across diverse experimental settings.

Model performance evaluation

To assess model performance, we employed a 5-fold cross-validation approach, where images from each individual data set as well as an aggregate data set consisting of mixed images across data sets were used (Fig. 2). We assessed the F1 score across different datasets to determine the consistency and robustness of mitochondrial segmentation performance (Fig. 3). The heatmap reveals variations in F1 scores for each dataset, with the PIM001-P PDX model achieving the highest score on its corresponding test dataset (F1=0.85), and the Mix model matching or surpassing the scores of the *Drp1* KO, HCI-010, and PIM001-P models (0.82, 0.62, and 0.85 respectively), indicating strong alignment between model predictions and manual annotations (Fig. 3A). By contrast, the HCI-010 model achieved a low score (0.61), suggesting that dataset-specific characteristics can significantly affect model performance. Fig. 3B shows receiver operating characteristic (ROC) and precision-recall (PR) curves for evaluating the Mix model on each set of test samples. Given the unbalanced nature of the segmentation problem, the PR curves are most suitable for model evaluation, with AUC scores of 0.82, 0.70, and 0.86 for the *Drp1* KO, HCI-010, and PIM001-P models, respectively-results that align closely with the F1 scores (Fig. 3B).

To further evaluate the model's predictive accuracy, we visually compared the model's segmentation output with manual annotations for sample images across the datasets. Representative images where mitochondria identified by manual annotation (blue) and model prediction (red) are overlaid (magenta) in the "composed" panels, highlighting regions of concordance and minor

discrepancies (Fig. 3C). Overall, the model successfully identified the majority of mitochondria, aligning with quantitative results, and demonstrating its ability to reliably detect mitochondrial structure under varied experimental conditions. Despite some challenges in specific datasets, these findings underscore the model's broad applicability for large-scale mitochondrial morphology analysis, particularly when dealing with mixed or heterogeneous image sets.

In vitro cell models provide biological validations of the algorithm

We sought biological validation of our model with two approaches. First, we genetically manipulated a canonical mitochondrial structure regulator to test the AI's ability to discern an expected structural difference. Specifically, we conducted TEM of murine skeletal primary cells that were either wild type or engineered to lack the fission protein Drp1 (*Drp1* KO). Micrographs were analyzed at a resolution of 0.0075 μm/pixel. Our data demonstrated a statistically significant increase in elongation (where a value of 1 represents a perfect circle and higher values indicate more elongated shapes) in *Drp1* KO cells (2.64 ± 1.34) compared to the wild-type control group (2.05 ± 0.92) (Fig. 4B), consistent with the well-established role of Drp1 in driving mitochondrial fission. A significant increase in mitochondrial area was also observed in *Drp1* KO cells (0.26 ± 0.21 μm^2) compared to the control group (0.16 ± 0.16 μm^2) (Fig. 4B). These findings highlight the ability of our model to effectively capture and quantify expected mitochondrial morphological differences.

As a second biological validation, we examined micrographs from drug-treated samples for which we had previously established mitochondrial structure alterations using a variety of methods and functional characterizations[8]. We previously reported that different types of standard chemotherapies impact mitochondrial morphology of TNBC cells in distinct ways: DNA-damaging chemotherapy induced mitochondrial elongation, while taxanes, which disrupt microtubule dynamics, caused a decrease or no change in mitochondrial elongation (Fig. 5A)[8]. Consistent with those findings, our model detected a significant increase in elongation in MDA-MB-231 cells treated with doxorubicin (DXR) or carboplatin (CRB) (2.15 ± 0.94 and 2.12 ± 0.92, respectively) alongside increased area (0.16 ± 0.15

and 0.17 ± 0.17 μm²), compared to vehicle (VEH) (2.04 ± 0.97 in elongation, 0.16 ± 0.16 μm² in area) (Fig. 5B). In contrast, treatment with taxanes paclitaxel (PTX) and docetaxel (DTX) resulted in decreased mitochondrial elongation (2.00 ± 0.86 and 1.83 ± 0.69, respectively) and area (0.10 ± 0.08 and 0.13 ± 0.13 μm², respectively), compared to VEH (2.04 ± 0.97 in elongation and 0.16 ± 0.16 μm² in area) (Fig.5B). Together, these findings validate our model's ability to detect expected biological changes and highlight its potential for broader discovery applications.

Mitochondrial structure changes upon chemotherapy treatment observed in PDX models

We next sought to investigate whether our approach could detect changes in mitochondrial features, for which we did not have a priori knowledge, during clinically relevant biological transitions in TNBC using orthotopic PDX models. These models are well-known to recapitulate metastatic[37] and therapeutic resistance[8,15 38] phenotypes that match the originating patient tumors. We treated five unique PDX models with the conventional taxane DTX. Tumors in these five models exhibited varying degrees of responses to DTX (Fig. 6A), as expected based on heterogeneity of chemotherapy efficacy common amongst TNBC patients. We collected mammary tumors from mice that had been untreated (n= 1-3 per group) or had been administered DTX (n=1-3 per group) and processed samples for TEM followed by automated mitochondrial analysis using our algorithm. In four out of five PDX models, we observed decreased mitochondrial elongation following DTX treatment, with BCM-2147 showing a significant reduction ($p<0.0001$). This was accompanied by a decrease in mitochondrial area. In contrast, HCI-010, which exhibited the highest baseline elongation, showed a slight, non-significant increase in both elongation and area (Fig.6B). Representative micrographs illustrate these findings: DTX-treated cells exhibited shorter, more fragmented mitochondrial structures compared to untreated cells in BCM-2147 (Fig. 6C). Additionally, in tumors with greater baseline mitochondrial elongation, we detected a more pronounced reduction in elongation after DTX treatment, suggesting that initial mitochondrial morphology may influence the extent of structural and functional adaptations they undergo (Fig.6D). Indeed, our prior study provided functional evidence that a transition towards mitochondrial fragmentation causes reduced OXPHOS in TNBC cells[8]. We did not observe any clear

association between mitochondrial features and degree of DTX induced change in tumor volume (Fig.6A and B).

Mitochondrial structure changes upon metastasis observed in a PDX model

We selected a highly metastatic PDX model, PIM056, derived from a previously untreated TNBC patient. In this model, all mice bearing PIM056 primary tumors in the mammary fat pad (MFP) developed multiple macro-metastatic lung lesions within 16 weeks of MFP engraftment without the need for survival tumor resection surgery. Approximately 16 weeks post engraftment, when the mammary tumors measured on average 1000 mm^3, we collected matched MFP tumors and macro-dissected lung metastases from four individual mice (Fig.7A). TEM followed by automated mitochondria detection revealed significantly shorter mitochondria in lung metastases compared to mammary tumors (Fig. 7). This finding was consistent across all four mice, aligning with a recent report of HER2+ breast cancer models that reported increased mitochondrial fission in lung metastases relative to MFP tumors[39]. The functional relevance of mitochondrial length in TNBC metastasis will be an important topic for future investigations.

DISCUSSION

The application of AI is advancing the field of biomedical image analysis[40]. Traditional manual annotation of cancer images is labor-intensive, prone to human bias, and often inconsistent between analysts, platforms, and institutions, making large-scale studies impractical. The AI-driven model presented here addresses these limitations by automating the detection and characterization of mitochondrial morphology with high accuracy and consistency. A key contribution of our AI model is its capacity to capture and quantify the heterogeneity and dynamics of mitochondrial morphology in biologically important transitions.

Chemotherapy-induced changes in mitochondrial structure are crucial indicators of cellular adaptation mechanisms, including metabolic reprogramming and resistance to cell death. Notably, our prior work demonstrated that genetically or pharmacologically inducing mitochondrial fission or fusion

was sufficient to modulate OXPHOS and chemotherapeutic responses[8]. By detecting subtle changes in structural features across large datasets, our approach provides new insights into how mitochondria may contribute to the survival of residual cancer cells post-treatment. We expect our model and highly curated annotations may not only accelerate the analysis of large datasets but may also enable a level of statistical rigor that is difficult to achieve with manual methods. Its robustness, stemming from training on a diverse set of images, underscores its potential for broad applicability in various biological contexts. To benefit the research community, we have made both our algorithm code and our extensive collection of TEM images publicly available. This dataset includes 125 micrographs with a total of 11,039 mitochondrial annotations, which we anticipate will serve as a valuable resource for developing further AI-driven analysis tools.

We observed substantial intra-tumor heterogeneity of mitochondrial shapes and sizes within individual micrographs from both cell lines and PDX models (Supplementary Fig. 1). Although genomic, transcriptomic, epigenomic, and proteomic heterogeneity are well-established phenomena across diverse cancers, including within the cell models in this study, the diversity of mitochondrial structure has only recently begun to gain attention in cancer[41,42]. Our algorithm's ability to capture this heterogeneity with high resolution, even within a decades-old, well-established human cell line, suggests an important, previously underappreciated layer of complexity in cancer cell biology. These observations raise compelling questions about how variations in mitochondrial morphology may correlate with functional differences or therapy responses, underscoring the need for deeper investigation into the potential role of mitochondrial heterogeneity in tumor progression.

Our study has several limitations. First, PDX models lack a fully intact immune system, which may be important for mitochondrial features of tumor cells. Consequently, extending our algorithm to immune-competent mouse tumor models will be crucial. Second, the generalizability of our observed chemotherapy-induced mitochondrial structure changes should be further assessed in additional *in vitro* and *in vivo* models with additional conventional chemotherapies, and ideally in human tumor specimens. This is especially important given the well-established inter-patient heterogeneity of TNBC[43-45]. Our

algorithm is precisely designed to enable such high-throughput analyses on large sample sets. Third, TEM provides only a two-dimensional cross section of mitochondria and is unable to capture their full three-dimensional complexity[42]. We hypothesize that analyzing high numbers of mitochondria, representing a random sampling of cells' cross-sections, as presented in this study, may mitigate this limitation by approximating the "average" morphological properties within each sample.

While our current analysis focused exclusively on mitochondrial morphology, a more holistic understanding of the chemotherapy-induced cellular changes will require analyzing other organelles, such as the nucleus, cell membrane, lipid droplets, and endoplasmic reticulum, that can have important interactions with mitochondria. These organelles play significant roles in cellular metabolism, signaling, and overall homeostasis in concert with mitochondria and may be important contributors to therapeutic resistance in cancer.

FIGURE LEGENDS

Figure 1. Schematic overview of the UNet AI pipeline for mitochondrial segmentation and analysis. The workflow begins with the preparation of training data, including transmission electron micrographs and manually annotated masks of mitochondria. Images are then rescaled to a common resolution (0.0075μm/pixel) and divided into smaller tiles for input into the neural network. Data augmentation, such as rotations, flips, and brightness adjustments, enhances model robustness to image variability. The UNet architecture, consisting of contracting and expanding paths, is trained to generate segmentation maps from the input image tiles. Following training, the model is used to make predictions on new images, with segmentation masks stitched together for full-image analysis. Downstream analysis includes computer vision tasks for feature quantification and statistical evaluations of mitochondrial morphology across experimental conditions.

Figure 2. Evaluation of model performance using 5-fold cross-validation across datasets. The datasets include *Drp1* KO, HCI-010, PIM001-P, and a mixed dataset combining samples from all groups.

The cross-validation approach divided each dataset into five groups, with one group used for testing and the remaining groups for training in each fold. Line plots on the right display F1 scores for each fold during training, demonstrating convergence and model performance across datasets. Consistent F1 score trends across folds indicate reliable segmentation performance, with variations reflecting dataset-specific characteristics. The mixed dataset exhibited robust generalizability, capturing diverse image features and achieving high performance.

Figure 3. Evaluation of segmentation performance and visual comparison of model predictions. (A) The heatmap in the top panel presents F1 scores across datasets, highlighting dataset-specific performance variations. Models trained on PIM001-P and the mixed dataset achieved the highest F1 scores, demonstrating robustness in capturing mitochondrial features. (B) Receiver operating characteristic (ROC) and precision-recall (PR) curves for evaluating the Mix model on each set of test samples. Given the unbalanced nature of the segmentation problem, the PR curves are most suitable for model evaluation. (C) Representative micrographs compare manual annotations (blue), model predictions (red), and overlapping regions (magenta).

Figure 4. Genetic validation of model performance. (A) The top panel presents representative micrographs of mitochondria from wild-type (WT) and *Drp1* knockout (KO) murine skeletal muscle cells. Arrows indicate elongated mitochondria in *Drp1* KO cells, consistent with reduced mitochondrial fission. (B) Box plots of mitochondrial elongation (left) and area (right) for WT and *Drp1* KO cells. Boxplots include sample sizes (WT: 1318; KO: 373 mitochondria). Data are represented as the mean ± SD. Scale bars are 0.2 μm. ****$P < 0.0001$, ***$P<0.001$ by two-tailed *t*-test.

Figure 5. Pharmacologic validation of model performance. (A) Representative micrographs from MDA-MB-231 cells were treated with VEH, DXR, CRB, PTX, or DTX. (B) Box plots of mitochondrial elongation (left) and area (right) for each treatment condition are displayed. Data are represented as the mean ± SD. Boxplots include sample sizes (vehicle: 1161; DXR: 1671; CRB: 1252; PTX: 619; DTX: 850 mitochondria). Scale bars are 0.2 μm. ****$P < 0.0001$, ***$P < 0.001$ by two-tailed *t*-test.

Figure 6. Analysis of mitochondrial changes in PDX models treated with DTX. (A) Line plots showing normalized tumor volume over time in five PDX models treated with DTX (starting on Day 0) compared to untreated controls. Red arrows on the x-axis indicate each administered DTX dose. (B) Box plots summarize mitochondrial elongation and area across the five PDX models. Data are represented as the mean ± SD, with sample sizes indicated for each group. Scale bars=0.2 μm. ****$P < 0.0001$, **$P < 0.01$ by two-tailed *t*-test statistical analysis.

Figure 7. Mitochondrial morphology differences between mammary tumors and lung metastases (A) Schematic representation of the PIM056 PDX model (top), where tumors were allowed to grow for 16 weeks before isolation of both primary mammary fat pad (MFP) tumors and lung metastases for analysis. Representative TEM images show mitochondrial structures in MFP (middle) and lung metastases (bottom). Scale bars=0.2 μm. (B) Box plots of mitochondrial elongation (left) and area (right) in lung metastases compared to primary tumors. Data are represented as the mean ± SD. Sample sizes are provided for each group (primary: 27,286; metastases: 25,226 mitochondria). Scale bars=0.2 μm. ****P < 0. by two-tailed *t*-test.

METHODS

TNBC cell culture and drug treatment The MDA-MB-231 cell line was purchased directly from ATCC (American Type Culture Collection) and cultured in RPMI-1640 (Gibco, 11879020) supplemented with 5 mM glucose (Gibco, A2494001), 10% fetal bovine serum (FBS) (R&D, S11550), and 1× antibiotic-antimycotic solution (Corning, 30-004-CI). Except for carboplatin (solutions were freshly prepared from powder), we prepared stock solutions of 10 mM in DMSO, and further dilutions were prepared in a proper growth medium. Cells were seeded at ~20% confluence and maintained for 48 h before treatment. Cells were then treated with: doxorubicin (final conc. at 100 nM, Sigma-Aldrich, 44583, protected from light), carboplatin (final conc. at 100 μM, Selleck Chemicals, S1215), paclitaxel (final conc. at 10 nM, Selleck Chemicals, Houston TX, S1150) or docetaxel (final conc. at 5 nM, Selleck Chemicals, Houston TX, S1148) for 48 hours before fixation.

Validation of cell lines and PDX models Cell cultures were tested for mycoplasma contamination each quarter using PCR with the Universal Mycoplasma Detection Kit (ATCC, 30-1012K), and were confirmed to be mycoplasma-free throughout the duration of this study. Short-tandem repeat (STR) DNA fingerprinting was performed on DNA extracted from both cell lines and PDX model tumors by the Cytogenetics and Cell Authentication Core (CCAC) at M.D. Anderson Cancer Center. The Promega 16 High Sensitivity STR Kit (Catalog # DC2100) was used for the fingerprinting analysis, and the resulting profiles were compared against online search databases (DSMZ, ATCC, JCRB, RIKEN) for authentication.

Animal studies This study was carried out in accordance with the *Guide for the Care and Use of Laboratory Animals* from the National Institutes of Health (NIH) IACUC. The protocol was approved by the IACUC at BCM (protocol AN-8243 and AN-2289). Mice were euthanized when they reached defined study or ethical end points. Euthanasia was conducted as recommended by the Association for Assessment and Accreditation of Laboratory Animal Care International. PIM001-P, PIM005[15] and PIM056[34] were propagated as previously described[1]. Briefly, cryo-preserved PDX cell suspensions were quickly thawed, then washed with Dulbecco's modified Eagle's medium (DMEM):F12 (Cytiva HyClone, SH30023.01) supplemented with 5% FBS. Viable cells were counted by staining with AOPI dye (Nexcelom Bioscience, CS2-0106) on a Cellometer K2 (Nexcelom Bioscience). For injection into mammary glands, 0.5-1.0 million viable tumor cells were suspended in a total of 20 µl (1:1 volume mixture of medium and Matrigel (Corning, 354234). Suspensions were then immediately injected unilaterally into the fourth mammary fat pads of 5 to 8-week-old female NOD/SCID [NOD.CB17-Prkdc^{scid}/NcrCrl, Charles River, National Cancer Institute (NCI) Colony] or NRG [NOD-Rag1null IL2rgnull] mice (Envigo). For HCI-010, BCM-2147, BCM-15116, and WHIM-14, cryo-preserved tumor fragments (1-2mm^3) were quickly thawed and washed with DMEM. The tumor chunks were orthotopically xenografted to 4th mammary gland of 6-8-week-old SCID/beige female mice.

Chemotherapy treatment of PDX models was conducted as previously described. Docetaxel solutions were administered by intraperitoneal injection at 20 mg/kg.

For PIM056 metastasis studies, lung metastases and mammary tumors were collected immediately following euthanasia when primary tumors reached approximately 1200 mm^3. Macro-metastatic lesions visual to the naked eye were isolated with scalpels then preserved for TEM as below.

To generate *Drp1* KO skeletal muscle murine myotubes, mouse husbandry was carried out in accordance with standard protocols[46] approved by the University of Iowa IACUC. Male C57Bl/6J mice were housed at 22 °C with a 12 h light, 12 h dark cycle and free access to water and standard chow. Controls represent pure C57Bl/6J genetic background mice. In accordance with previous studies[47-49], Tamoxifen-inducible, skeletal muscle-specific *Drp1* KO mice were generated by crossing mice carrying a homozygous floxed allele of *Drp1* with mice carrying a tamoxifen-inducible Cre recombinase under the control of the skeletal muscle-specific myogenin promoter (Jackson Lab).

Isolation of satellite cells and differentiation To collect tissue samples from wild-type or *Drp1* KO mice, animals were anesthetized using isoflurane at 8–10 weeks old. Skeletal muscles from the gastrocnemius and quadriceps were excised and washed twice with 1x phosphate-buffered saline (PBS) supplemented with 1% penicillin-streptomycin and 0.3% fungizone (300 μL/100 mL The muscles were then incubated in Dulbecco's Modified Eagle's Medium (DMEM)-F12 containing 0.2% collagenase II (2 mg/mL), 1% penicillin-streptomycin, and 0.3% fungizone (300 μL/100 mL). Samples were shaken for 90 minutes at 37 °C. Following incubation, the media was removed, and the muscle tissue was washed four times with PBS. The media was then replaced with DMEM-F12 containing 0.05% collagenase II (0.5 mg/mL), 1% penicillin-streptomycin, and 0.3% fungizone (300 μL/100 mL), followed by shaking for 30 minutes at 37 °C. Post-digestion, the tissue was ground until cells were dislodged from the tissue matrix and then passed through a 70 μm cell strainer. The isolated cells were centrifuged, resuspended, and plated on BD Matrigel-coated dishes. Adherent cells were differentiated into myotubes by adding DMEM-F12, 20% FBS, 0.004% (40 ng mL-1) basic fibroblast growth factor (R&D Systems, 233-FB/CF), 1× non-essential amino acids, 0.14 × 10^3 m β-mercaptoethanol, 1x penicillin/streptomycin, and 0.3% fungizone (300 μL/100 mL). Myotubes were maintained in a medium containing 0.001% (10 ng/mL)

growth factor until reaching 85% confluency, then were differentiated in DMEM-F12, 2% FBS, and 1× insulin-transferrin-selenium.

Transmission electron microscopy (TEM) Tumor cells were fixed, processed, and embedded in situ to prevent morphological damage, as follows. Cells were fixed for 24 hours in Karnovsky's fixative, post-fixed in 1% osmium tetroxide, dehydrated in graded ethanol, and embedded in EMbed 812 resin. Ultra-thin sections were cut using a Leica UC7 ultramicrotome, stained with saturated methanolic uranyl acetate and Reynold's lead citrate, and imaged using a JEOL JEM-1230 TEM equipped with an AMT NanoSprint15 sCMOS camera. For tumor tissues, immediately following ethical animal euthanasia, mammary tumors were resected from mice and a ~1 mm-tick tumor slice was placed in Trump's fixation solution and fixed for 24 hours at room temperature with rocking. The necrotic areas that usually found in the core region of solid tumors were avoided. The initial fixed samples then were post-fixed in 1% buffered osmium tetroxide, dehydrated in graded ethanol, and embedded in Polybed 812 resin. Ultra-thin sections were obtained using a Leica UC 7 and sections were stained in 1% aqueous uranyl acetate and Reynold's lead citrate. Images were obtained using a FEI Tecnai Spirit TEM equipped with an Eagle camera and FEI Tia image acquisition software. Approximately 65 images at magnifications of 400-5000x were taken per tumor sample.

Myotubes were processed for TEM in accordance with previous studies[50,51]. For 1 h, cells were fixed by incubating at 37 °C with 2.5% glutaraldehyde in 0.1 m sodium cacodylate buffer. After rinsing twice with 0.1 m sodium cacodylate buffer, samples were fixed again at room temperature for 30 min to 1 h using 1% osmium tetroxide and 1.5% potassium ferrocyanide in 0.1 m sodium cacodylate buffer.

After secondary fixation, samples were washed for 5 min with 0.1 m sodium cacodylate buffer (7.3 pH). From there, two washings of 5 min with diH_2O ensured the plates were cleaned. While keeping all solutions and plates at room temperature, the samples were incubated with 2.5% uranyl acetate, diluted with H_2O, at 4 °C overnight. Following this, samples were dehydrated using an ethanol gradient series. After dehydration, the ethanol was replaced with Eponate 12 mixed in 100% ethanol in a 1:1 solution,

then incubated at room temperature for 30 min. This was repeated three times for 1 h using 100% Eponate 12. The plates were finally placed in new media and cured in an oven at 70 °C overnight.

Plates were cracked upon hardening, and the cells were separated by submerging the plate in liquid nitrogen. An 80 nm thickness jeweler's saw was used to cut the block to fit in a Leica UC6 ultramicrotome sample holder. From there, the section was placed on formvar-coated copper grids. These grids were counterstained in 2% uranyl acetate for 2 min. Then these grids were counterstained by Reynold's lead citrate for 2 min. Images were acquired by TEM on either a JEOL JEM-1230, operating at 120 kV, or a JEOL 1400, operating at 80 kV.

Manual annotation of micrographs For each tumor or cell line, 50-60 transmission electron micrographs were obtained at different magnifications, ranging from 1000X to 5000X magnification. These micrographs were then loaded into the QuPath software[33], a versatile tool for bioimage analysis. Each mitochondrion within the micrographs was manually annotated using the drawing tool provided by QuPath. This process involved carefully outlining the boundaries of individual mitochondria to ensure precise and accurate characterization of their morphological features. The manual annotations were subsequently used for further analysis, providing a detailed dataset for evaluating mitochondrial structure across various tumor samples.

Model A UNet model was utilized to perform semantic segmentation on the TEM images. This deep-learning model is an autoencoder that consists of a feature extraction stage (contracting path, encoder) and a reconstruction stage (expansive path, decoder). The model uses a series of convolutional and max pooling layers to transform the input image into abstract features in a latent space, that will then be decoded in the reconstruction stage to match the model output with the corresponding training mask. A defining characteristic of a UNet model is the use of feature maps from the contracting path, as input features in the expansive path. This choice helps to localize and assemble a more precise output mask[31]. The network architecture is described in the following. The 2D input layer is followed by a Gaussian Noise layer with standard deviation of 0.01. Each convolutional layer has kernel size 3 and

is followed by a leaky ReLu activation layer, a 2D spatial dropout layer (rates 0.2 and 0.1 in the contracting and expansive paths respectively), and a batch normalization layer. A convolutional block is composed of two such convolutional layers, followed by either a 2 by 2 max pooling layer in the contracting path, or a 2 by 2 up-convolution layer with stride 2 in the expanding path. The model is composed of 9 convolutional blocks in total: 4 in the contracting path, 1 in the bottleneck, and 4 in the expansive path. The first convolutional block uses 16 filters in each of its convolutional layers. The number of filters used in the convolutional layers doubles after each max pooling layer, and halves after each up-convolution layer. The full model has just under 2 million trainable parameters.

Datasets Three different datasets were used for training four U-Net models. The datasets are labeled as *Drp1* KO, HCI-010, and PIM001-P, with 26, 21, and 37 images respectively. The *Drp1* KO dataset contains images from the control set of an *in vitro* genetically engineered mouse myotube model. HCI-010 and PIM001-P contain images from two corresponding *in vivo* PDX mouse models. All images in the training datasets correspond to non-perturbed (control/vehicle) samples. For each dataset, a model was trained. A mixed model was also trained using images from these three datasets, along with control images of 3 other datasets (BCM-2147, MDA-MB-231, and PIM005), using a total of 125 images for training.

Preprocessing training data The training dataset consists of electron micrographs, each paired with a manually annotated segmentation mask indicating the mitochondria. Magnification information was parsed from the image to obtain its resolution in pixels/μm. Images were scaled to match a common resolution of 133 pixels/μm. Each image-mask pair was tiled to appropriately sized input samples that fit the model architecture shape (444 by 444 in the input layer, and 260 by 260 pixels at the output). The tiled process was performed in an overlapping fashion with a stride of 130 pixels in both horizontal and vertical directions. To avoid losing the pixels at the border, the images were zero-padded. The pixel values are rescaled to lie in the range [0,1]. The tile sets were converted into TF records to improve

training computational performance. The final output was assembled by stitching the overlapping predicted mask tiles and taking the average for the overlapping regions.

Data augmentation During model training, the input tiles were randomly transformed by rotating and flipping the images. This step was performed to increase the number of training samples and to avoid orientation bias. Moreover, the brightness, contrast and gamma image parameters were randomly adjusted to account for variation of these parameters across the input images. Additionally, images were randomly magnified to boost the robustness of the model to input image resolution.

Model training The model was trained on Nvidia DGX-A100 GPUs, for a total of 1200 epochs and batch size 128. The Adam optimizer was used with the default parameters, and a weighted binary cross entropy loss function, assigning double weight to positive mask pixels. Model checkpoints were saved for the best achieved loss on the validation sets. The convergence of the model was monitored using the corresponding loss metric, as well as the IOU and DICE coefficients.

Performance evaluation The data was split into a training set and a test set (85% and 15% approximately). A 5-fold cross validation was used in the training set, where each fold uses 4 subsets for training and the remaining 5th set as validation. Model performance was assessed using the left-out test set.

Model predictions Each of the 5 resulting models from the cross-validation procedure were used to make predictions on new images. An ensemble approach was used to aggregate the results in a single prediction, by taking the average of all predictions.

Statistical analysis Statistical differences in mitochondrial features between treatment groups was performed using a two tailed *t*-test with the Statsmodels Python package[52].

Data and code availability Cell line models of TNBC are available for purchase from ATCC. PDX models can be made available to investigators through a material transfer agreement with the University of Texas MD Anderson Cancer Center (PIM001-P, PIM005 and PIM056) or Baylor College of Medicine

(HCI-010, BCM-2147, BCM-15116, and WHIM-14). The Python code will be made available on GitHub (DOI pending). Electron micrographs and annotated mitochondrial masks are currently being deposited on The Cancer Imaging Archives (TCIA) and are available upon request.

AUTHOR CONTRIBUTIONS

A.A., L.M.B., K.Z., and G.V.E were responsible for overall completion of the study, writing the manuscript, and preparation of figures.

L.M.B., K.Z., and G.V.E were responsible for project conceptualization.

L.M.B. conducted PDX and cell line experiments, generated electron micrographs, conducted manual annotations of mitochondria, and data analyses under the supervision of G.V.E.

A.A. conducted computational algorithm development, optimization, and testing under the supervision of K.Z.

M.J.B. conducted PDX chemotherapy trials and generated electron micrographs analyzed in this study under the supervision of G.V.E.

A.Z. conducted initial algorithm development under the supervision of K.Z.

A.O.H. provided electron micrographs of WT and *Drp1*KO myotubes.

M.D.M. aided in design of electron microscopy imaging and generated most images in this study.

L.E.D. conducted PDX chemotherapy trials and provided tissues for electron microscopy under the supervision of M.T.L.

ACKNOWLEDGEMENTS

We are grateful to the breast cancer patients who donated their biopsies for cell line and PDX model generation. We are grateful to Mrs. Janice Cowden for providing advocacy support for our research. Dr.

James P. Barrish assisted with TEM. Dr. Junegoo Lee assisted with mouse experiments. Dr. Helen Piwnica-Worms provided the PIM001-P and PIM056 PDXs through MTA with the University of Texas MD Anderson Cancer Center, and model generation was supported by a generous gift from the Cazalot Foundation through the MD Anderson Women's Cancer Moonshot Program. STR DNA fingerprinting was done by the Cytogenetics and Cell Authentication Core at M.D. Anderson Cancer Center.

FUNDING

G.V.E. is a Cancer Prevention Research Institute of Texas (CPRIT) Scholar in Cancer Research. The authors are supported by CPRIT RR200009 to G.V.E., National Institutes of Health (NIH) R37CA269783-01A1 to G.V.E., R37CA269783-01A1 to K.Z., R01AI167570 to K.Z., American Cancer Society RSG-22-093-01-CCB to G.V.E, National Science Foundation 2140736 to M.J.B., and Baylor Research Advocates for Student Scholars (BRASS) Myra Branum Wilson Scholarship to M.J.B. The content is solely the responsibility of the authors and does not necessarily represent the official views of the NIH, NSF, CPRIT, ACS, or BRASS. BCM PDX core is supported by P30 Cancer Center Support Grant NCI-CA125123, CPRIT Core Facilities Support Grant RP220646.

REFERENCES CITED

1 Anderson, A. J., Jackson, T. D., Stroud, D. A. & Stojanovski, D. Mitochondria-hubs for regulating cellular biochemistry: emerging concepts and networks. *Open Biol* **9**, 190126, doi:10.1098/rsob.190126 (2019).

2 Rossmann, M. P., Dubois, S. M., Agarwal, S. & Zon, L. I. Mitochondrial function in development and disease. *Dis Model Mech* **14**, doi:10.1242/dmm.048912 (2021).

3 Nguyen, T. T. *et al.* Mitochondria-associated programmed cell death as a therapeutic target for age-related disease. *Exp Mol Med* **55**, 1595-1619, doi:10.1038/s12276-023-01046-5 (2023).

4 Mitra, K., Wunder, C., Roysam, B., Lin, G. & Lippincott-Schwartz, J. A hyperfused mitochondrial state achieved at G1-S regulates cyclin E buildup and entry into S phase. *Proc Natl Acad Sci U S A* **106**, 11960-11965, doi:10.1073/pnas.0904875106 (2009).

5 Egan, G. *et al.* Mitochondrial and Metabolic Pathways Regulate Nuclear Gene Expression to Control Differentiation, Stem Cell Function, and Immune Response in Leukemia. *Cancer Discov* **11**, 1052-1066, doi:10.1158/2159-8290.CD-20-1227 (2021).

6 Chen, W., Zhao, H. & Li, Y. Mitochondrial dynamics in health and disease: mechanisms and potential targets. *Signal Transduct Target Ther* **8**, 333, doi:10.1038/s41392-023-01547-9 (2023).

7 Raven, K. D. & Kapetanovic, R. Mitochondrial dynamics: Regulating cell metabolism, homoeostasis, health and disease. *Semin Cell Dev Biol* **161-162**, 20-21, doi:10.1016/j.semcdb.2024.02.002 (2024).

8 Baek, M. L. *et al.* Mitochondrial structure and function adaptation in residual triple negative breast cancer cells surviving chemotherapy treatment. *Oncogene* **42**, 1117-1131, doi:10.1038/s41388-023-02596-8 (2023).

9 Boulton, D. P. & Caino, M. C. Mitochondrial Fission and Fusion in Tumor Progression to Metastasis. *Front Cell Dev Biol* **10**, 849962, doi:10.3389/fcell.2022.849962 (2022).

10 Sessions, D. T. *et al.* Opa1 and Drp1 reciprocally regulate cristae morphology, ETC function, and NAD(+) regeneration in KRas-mutant lung adenocarcinoma. *Cell Rep* **41**, 111818, doi:10.1016/j.celrep.2022.111818 (2022).

11 Perou, C. M. Molecular stratification of triple-negative breast cancers. *Oncologist* **16 Suppl 1**, 61-70, doi:10.1634/theoncologist.2011-S1-61 (2011).

12 Symmans, W. F. *et al.* Long-Term Prognostic Risk After Neoadjuvant Chemotherapy Associated With Residual Cancer Burden and Breast Cancer Subtype. *J Clin Oncol* **35**, 1049-1060, doi:10.1200/JCO.2015.63.1010 (2017).

13 Yau, C. *et al.* Residual cancer burden after neoadjuvant chemotherapy and long-term survival outcomes in breast cancer: a multicentre pooled analysis of 5161 patients. *Lancet Oncol* **23**, 149-160, doi:10.1016/S1470-2045(21)00589-1 (2022).

14 Hamy, A. S. *et al.* Prognostic value of the Residual Cancer Burden index according to breast cancer subtype: Validation on a cohort of BC patients treated by neoadjuvant chemotherapy. *PLoS One* **15**, e0234191, doi:10.1371/journal.pone.0234191 (2020).

15 Echeverria, G. V. *et al.* Resistance to neoadjuvant chemotherapy in triple-negative breast cancer mediated by a reversible drug-tolerant state. *Sci Transl Med* **11**, doi:10.1126/scitranslmed.aav0936 (2019).

16 Herkenne, S. & Scorrano, L. OPA1, a new mitochondrial target in cancer therapy. *Aging (Albany NY)* **12**, 20931-20933, doi:10.18632/aging.104207 (2020).

17 Xie, L. *et al.* Drp1-dependent remodeling of mitochondrial morphology triggered by EBV-LMP1 increases cisplatin resistance. *Signal Transduct Target Ther* **5**, 56, doi:10.1038/s41392-020-0151-9 (2020).

18 Alalawy, A. I. *et al.* Inhibition of Drp1 orchestrates the responsiveness of breast cancer cells to paclitaxel but insignificantly relieves paclitaxel-related ovarian damage in mice. *Sci Rep* **13**, 22782, doi:10.1038/s41598-023-49578-0 (2023).

19 Noguchi, M. *et al.* Inhibition of the mitochondria-shaping protein Opa1 restores sensitivity to Gefitinib in a lung adenocarcinomaresistant cell line. *Cell Death Dis* **14**, 241, doi:10.1038/s41419-023-05768-2 (2023).

20 Decker, C. W. *et al.* Mitofusin-2 mediates doxorubicin sensitivity and acute resistance in Jurkat leukemia cells. *Biochem Biophys Rep* **24**, 100824, doi:10.1016/j.bbrep.2020.100824 (2020).

21 Rub, J. *et al.* A deep-learning tool for species-agnostic integration of cancer cell states. *bioRxiv*, 2024.2012.2020.629285, doi:10.1101/2024.12.20.629285 (2024).

22 Chaudhry, F., Kim, T. W., Elemento, O. & Betel, D. Machine learning analysis of population-wide plasma proteins identifies hormonal biomarkers of Parkinson's Disease. *medRxiv*, doi:10.1101/2024.12.21.24313256 (2024).

23 Wang, J. M. *et al.* Deep learning integrates histopathology and proteogenomics at a pan-cancer level. *Cell Rep Med* **4**, 101173, doi:10.1016/j.xcrm.2023.101173 (2023).

24 Suga, S. *et al.* An interactive deep learning-based approach reveals mitochondrial cristae topologies. *PLoS Biol* **21**, e3002246, doi:10.1371/journal.pbio.3002246 (2023).

25 Jiang, Y., Yang, M., Wang, S., Li, X. & Sun, Y. Emerging role of deep learning-based artificial intelligence in tumor pathology. *Cancer Commun (Lond)* **40**, 154-166, doi:10.1002/cac2.12012 (2020).

26 Noorbakhsh, J. *et al.* Deep learning-based cross-classifications reveal conserved spatial behaviors within tumor histological images. *Nat Commun* **11**, 6367, doi:10.1038/s41467-020-20030-5 (2020).

27 Yang, Y., Fang, Q. & Shen, H. B. Predicting gene regulatory interactions based on spatial gene expression data and deep learning. *PLoS Comput Biol* **15**, e1007324, doi:10.1371/journal.pcbi.1007324 (2019).

28 Rich, J. M. *et al.* Deep learning image segmentation approaches for malignant bone lesions: a systematic review and meta-analysis. *Front Radiol* **3**, 1241651, doi:10.3389/fradi.2023.1241651 (2023).

29 Xu, Y. *et al.* Advances in Medical Image Segmentation: A Comprehensive Review of Traditional, Deep Learning and Hybrid Approaches. *Bioengineering (Basel)* **11**, doi:10.3390/bioengineering11101034 (2024).

30 Yuan, J. Brain tumor image segmentation method using hybrid attention module and improved mask RCNN. *Sci Rep* **14**, 20615, doi:10.1038/s41598-024-71250-4 (2024).

31 Ronneberger, O., Fischer, P. & Brox, T. 234-241 (Springer International Publishing).

32 Farahmand, S. *et al.* Deep learning trained on hematoxylin and eosin tumor region of Interest predicts HER2 status and trastuzumab treatment response in HER2+ breast cancer. *Mod Pathol* **35**, 44-51, doi:10.1038/s41379-021-00911-w (2022).

33 Bankhead, P. *et al.* QuPath: Open source software for digital pathology image analysis. *Sci Rep* **7**, 16878, doi:10.1038/s41598-017-17204-5 (2017).

34 Echeverria, G. V. *et al.* Predictors of success in establishing orthotopic patient-derived xenograft models of triple negative breast cancer. *NPJ Breast Cancer* **9**, 2, doi:10.1038/s41523-022-00502-1 (2023).

35 Guillen, K. P. *et al.* A human breast cancer-derived xenograft and organoid platform for drug discovery and precision oncology. *Nat Cancer* **3**, 232-250, doi:10.1038/s43018-022-00337-6 (2022).

36 Zhang, X. *et al.* A renewable tissue resource of phenotypically stable, biologically and ethnically diverse, patient-derived human breast cancer xenograft models. *Cancer Res* **73**, 4885-4897, doi:10.1158/0008-5472.CAN-12-4081 (2013).

37 Echeverria, G. V. *et al.* High-resolution clonal mapping of multi-organ metastasis in triple negative breast cancer. *Nat Commun* **9**, 5079, doi:10.1038/s41467-018-07406-4 (2018).

38 Lei, J. T. *et al.* Patient-Derived Xenografts of Triple-Negative Breast Cancer Enable Deconvolution and Prediction of Chemotherapy Responses. *bioRxiv*, doi:10.1101/2024.12.09.627518 (2025).

39 Parida, P. K. *et al.* Limiting mitochondrial plasticity by targeting DRP1 induces metabolic reprogramming and reduces breast cancer brain metastases. *Nat Cancer* **4**, 893-907, doi:10.1038/s43018-023-00563-6 (2023).

40 Pinto-Coelho, L. How Artificial Intelligence Is Shaping Medical Imaging Technology: A Survey of Innovations and Applications. *Bioengineering (Basel)* **10**, doi:10.3390/bioengineering10121435 (2023).

41 Begum, H. M. *et al.* Spatial Regulation of Mitochondrial Heterogeneity by Stromal Confinement in Micropatterned Tumor Models. *Sci Rep* **9**, 11187, doi:10.1038/s41598-019-47593-8 (2019).

42 Han, M. *et al.* Spatial mapping of mitochondrial networks and bioenergetics in lung cancer. *Nature* **615**, 712-719, doi:10.1038/s41586-023-05793-3 (2023).

43 Fischer, J. R. *et al.* Multiplex imaging of breast cancer lymph node metastases identifies prognostic single-cell populations independent of clinical classifiers. *Cell Rep Med* **4**, 100977, doi:10.1016/j.xcrm.2023.100977 (2023).

44 Jovanovic, B. *et al.* Heterogeneity and transcriptional drivers of triple-negative breast cancer. *Cell Rep* **42**, 113564, doi:10.1016/j.celrep.2023.113564 (2023).

45 Lehmann, B. D. *et al.* Identification of human triple-negative breast cancer subtypes and preclinical models for selection of targeted therapies. *J Clin Invest* **121**, 2750-2767, doi:10.1172/JCI45014 (2011).

46 Pereira, R. O. *et al.* OPA1 deficiency promotes secretion of FGF21 from muscle that prevents obesity and insulin resistance. *EMBO J* **36**, 2126-2145, doi:10.15252/embj.201696179 (2017).

47 Favaro, G. *et al.* DRP1-mediated mitochondrial shape controls calcium homeostasis and muscle mass. *Nat Commun* **10**, 2576, doi:10.1038/s41467-019-10226-9 (2019).

48 Neikirk, K. *et al.* Systematic Transmission Electron Microscopy-Based Identification and 3D Reconstruction of Cellular Degradation Machinery. *Adv Biol (Weinh)* **7**, e2200221, doi:10.1002/adbi.202200221 (2023).

49 Southard, S. *et al.* A series of Cre-ER(T2) drivers for manipulation of the skeletal muscle lineage. *Genesis* **52**, 759-770, doi:10.1002/dvg.22792 (2014).

50 Lam, J. *et al.* A Universal Approach to Analyzing Transmission Electron Microscopy with ImageJ. *Cells* **10**, doi:10.3390/cells10092177 (2021).

51 Han, J. *et al.* ER-stress-induced transcriptional regulation increases protein synthesis leading to cell death. *Nat Cell Biol* **15**, 481-490, doi:10.1038/ncb2738 (2013).

52 Skipper Seabold, J. P. Statsmodels: Econometric and Statistical Modeling with Python. *SciPy Proceedings*, doi:https://doi.org/10.25080/Majora-92bf1922-011 (2010).

Figure 1

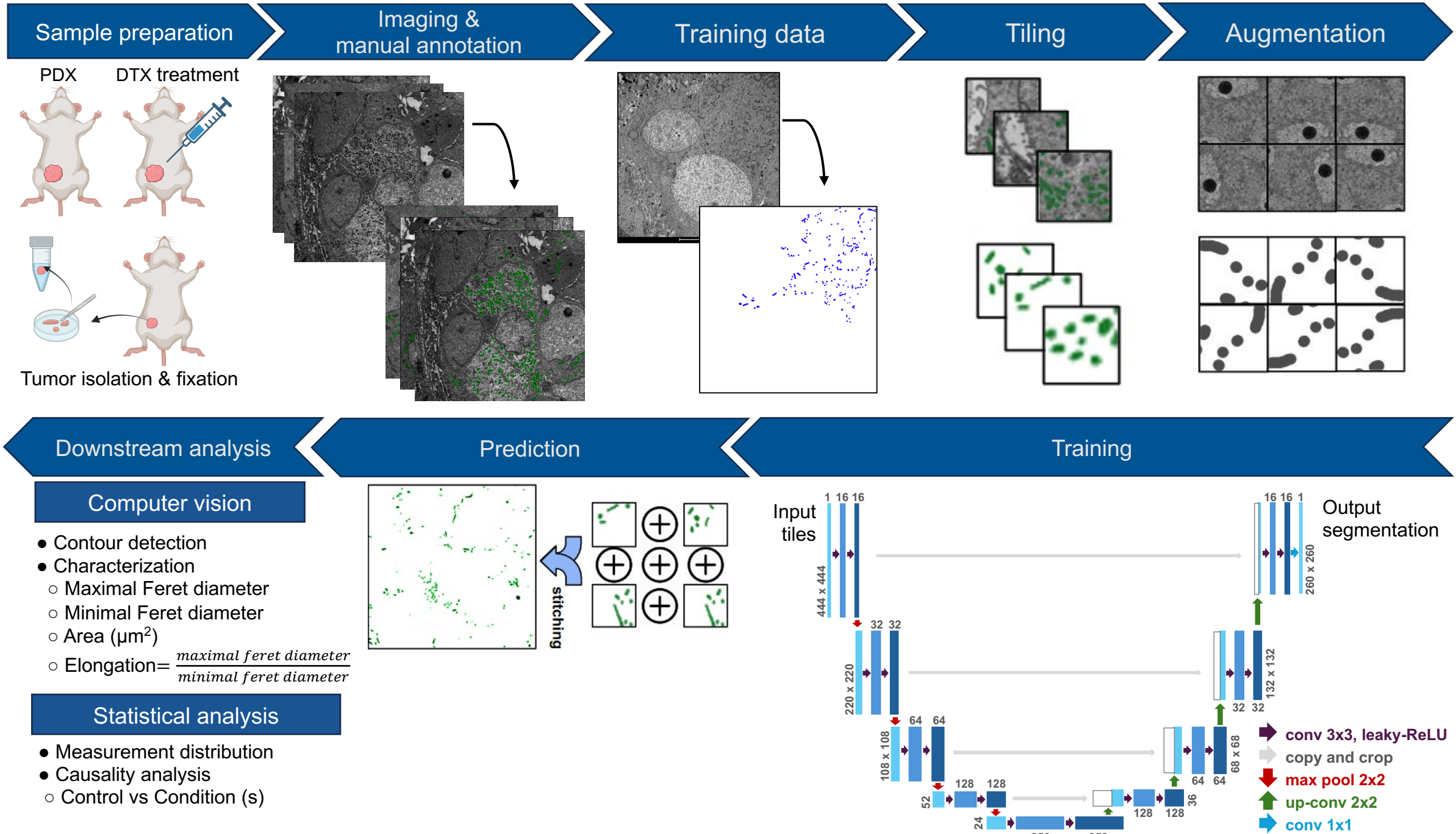
Sample preparation
Imaging & manual annotation
Training data
Tiling
Augmentation
PDX
DTX treatment
Tumor isolation & fixation
Downstream analysis
Prediction
Training
Computer vision
● Contour detection
● Characterization
○ Maximal Feret diameter
○ Minimal Feret diameter
○ Area (µm²)
○ Elongation= maximal feret diameter / minimal feret diameter
Statistical analysis
● Measurement distribution
● Causality analysis
○ Control vs Condition (s)
stitching
Input tiles
Output segmentation
conv 3x3, leaky-ReLU
copy and crop
max pool 2x2
up-conv 2x2
conv 1x1

Table 1

				Training + Validation				Test			
Model name	Training dataset(s)	Sample type	Species	# of images	Percent of fully annotated images	# of mitochondria	# of tiles	# of images	Percent of fully annotated images	# of mitochondria	# of tiles
Drp1 KO	*Drp1* KO	Cell line	Mouse	22	100%	766	5832	4	100%	80	1220
HCI-010	HCI-010	PDX Tumor	Human	17	100%	2401	43577	4	100%	106	1301
PIM001-P	PIM001-P	PDX Tumor	Human	32	100%	6099	32724	5	100%	1410	5280
Mixture	MDA-MB-231	Cell line	Human	125	40%	11039	124954	-	-	-	-
	Drp1 KO	Cell line	Mouse					-	-	-	-
	HCI-010	PDX Tumor	Human					-	-	-	-
	PIM001-P	PDX Tumor	Human					-	-	-	-
	PIM005-P	PDX Tumor	Human					-	-	-	-
	BCM2147	PDX Tumor	Human					-	-	-	-

Figure 2

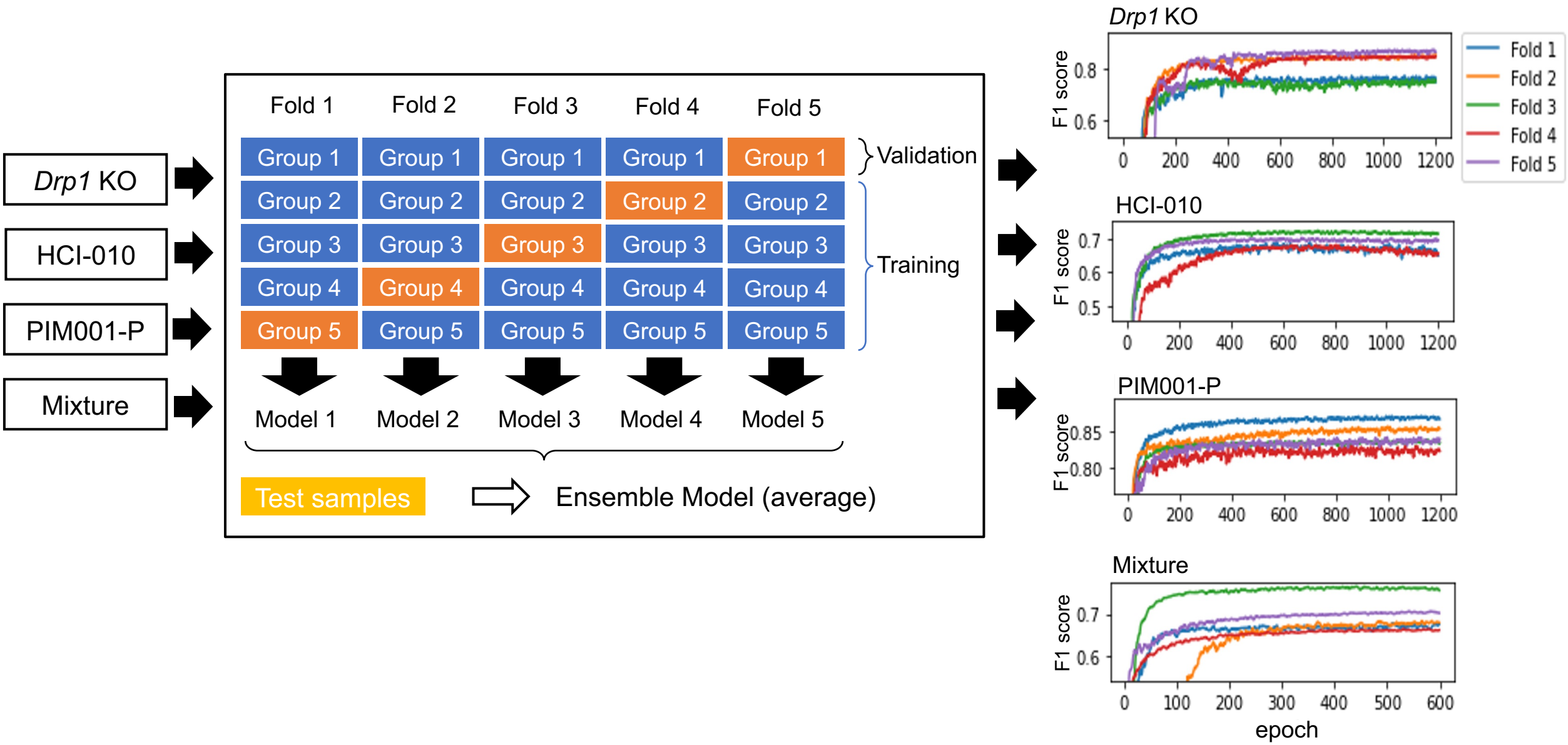
Drp1 KO
HCI-010
PIM001-P
Mixture
Fold 1
Fold 2
Fold 3
Fold 4
Fold 5
Group 1
Group 2
Group 3
Group 4
Group 5
Validation
Training
Model 1
Model 2
Model 3
Model 4
Model 5
Test samples
Ensemble Model (average)
Drp1 KO
HCI-010
PIM001-P
Mixture
F1 score
epoch
Fold 1
Fold 2
Fold 3
Fold 4
Fold 5

Figure 3

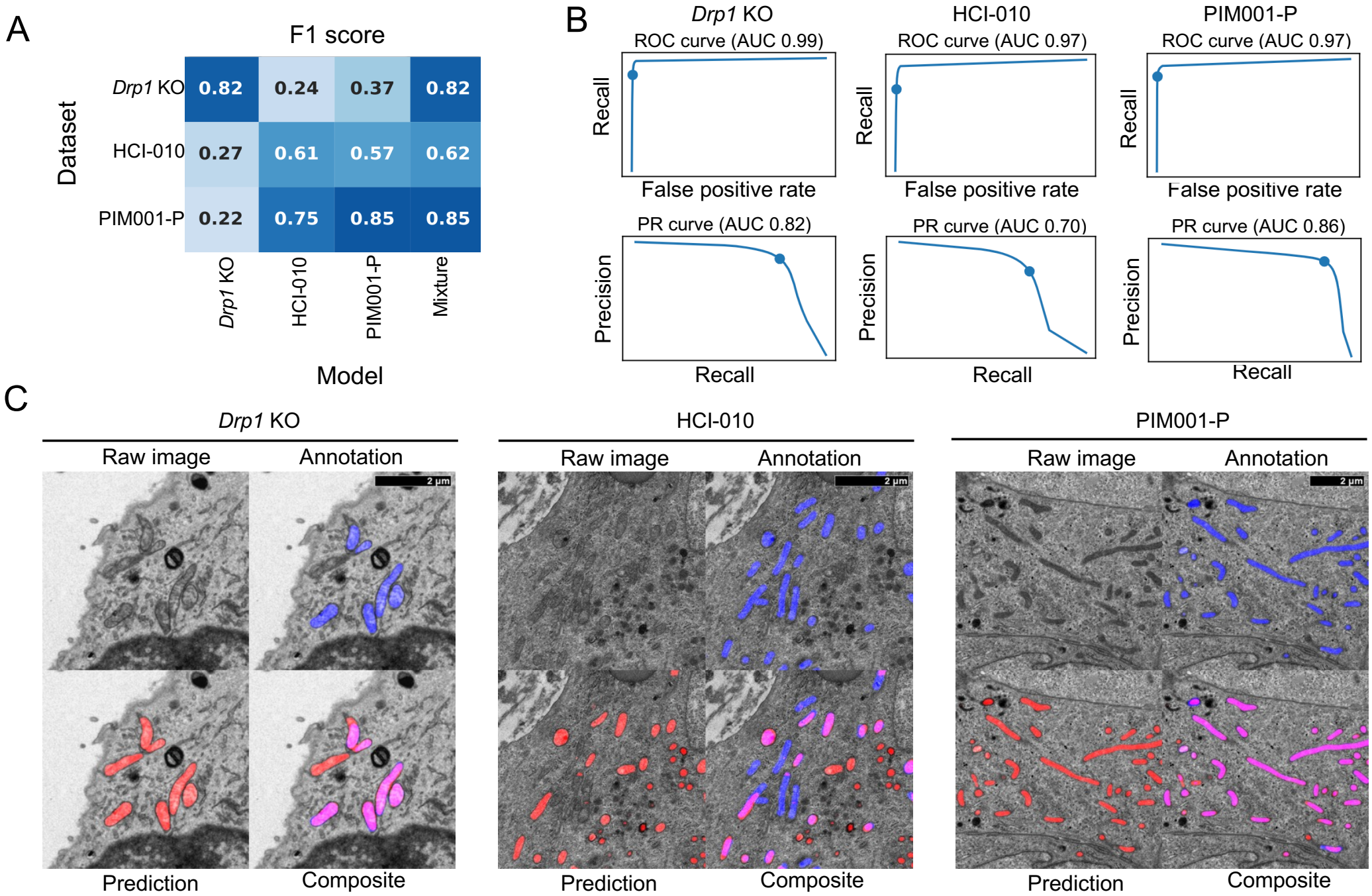
A
F1 score
Dataset
Drp1 KO 0.82 0.24 0.37 0.82
HCI-010 0.27 0.61 0.57 0.62
PIM001-P 0.22 0.75 0.85 0.85
Drp1 KO
HCI-010
PIM001-P
Mixture
Model
B
Drp1 KO
ROC curve (AUC 0.99)
HCI-010
ROC curve (AUC 0.97)
PIM001-P
ROC curve (AUC 0.97)
Recall
False positive rate
PR curve (AUC 0.82)
PR curve (AUC 0.70)
PR curve (AUC 0.86)
Precision
Recall
C
Drp1 KO
HCI-010
PIM001-P
Raw image
Annotation
2 µm
Prediction
Composite

Figure 4

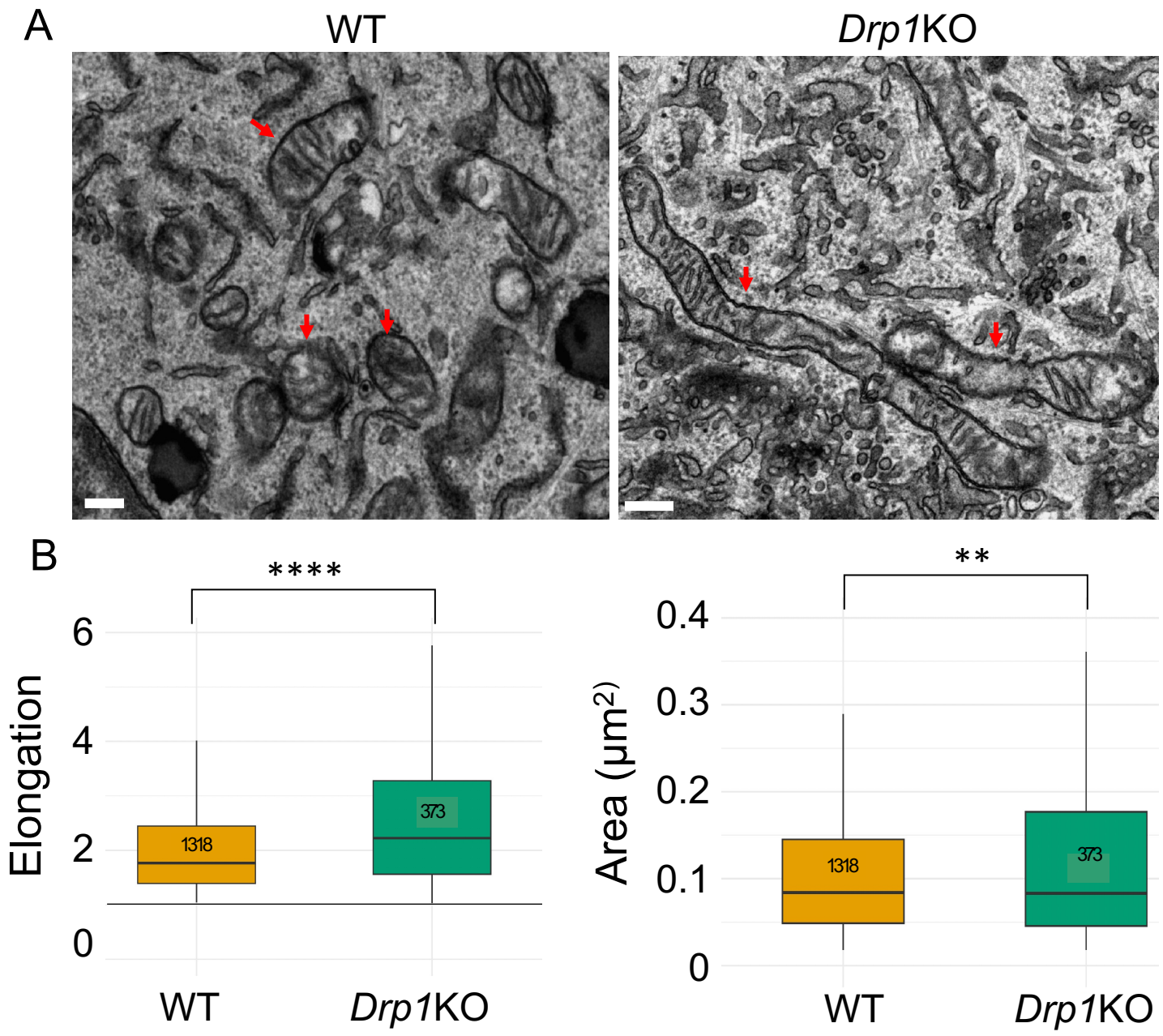
A
WT
Drp1KO
B
****
Elongation
6
4
2
0
1318
373
WT
Drp1KO
**
Area (μm²)
0.4
0.3
0.2
0.1
0
1318
373
WT
Drp1KO

Figure 5

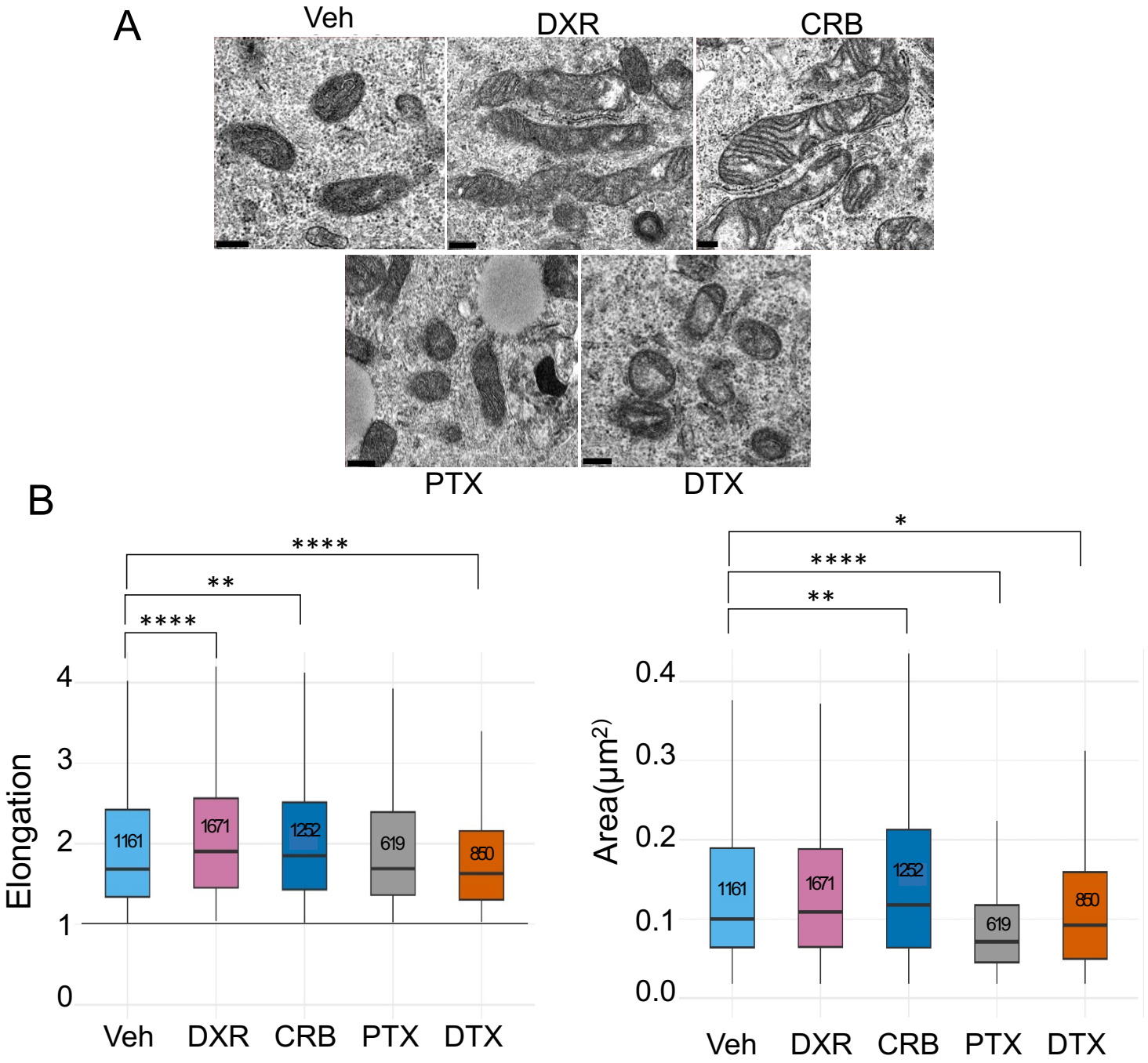
A
Veh
DXR
CRB
PTX
DTX
B
****
**
****
Elongation
4
3
2
1
0
1161
1671
1252
619
850
Veh
DXR
CRB
PTX
DTX
*
****
**
Area(μm²)
0.4
0.3
0.2
0.1
0.0
1161
1671
1252
619
850
Veh
DXR
CRB
PTX
DTX

Figure 6

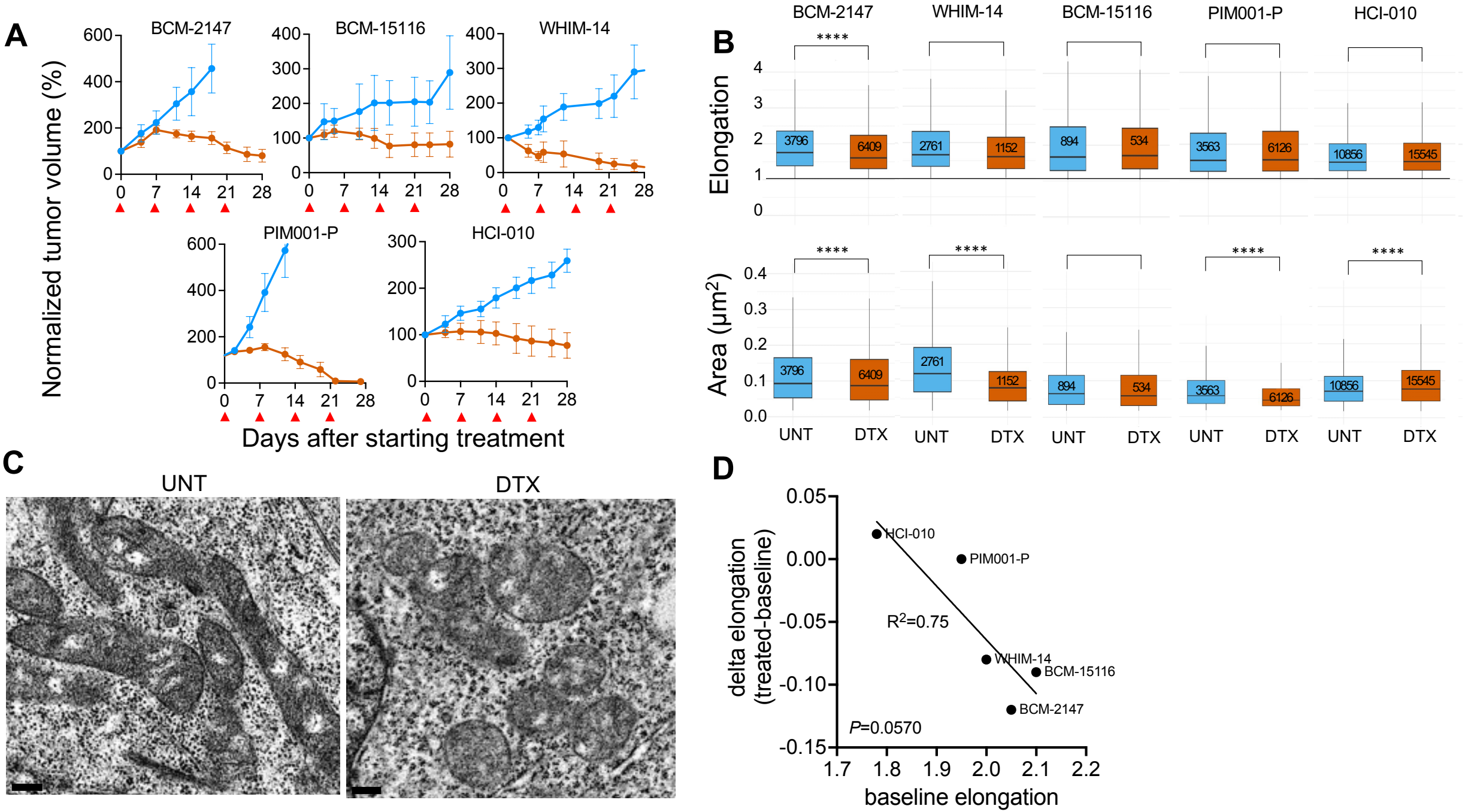
A
BCM-2147
BCM-15116
WHIM-14
PIM001-P
HCI-010
Normalized tumor volume (%)
Days after starting treatment
B
Elongation
Area (μm²)
****
3796
6409
2761
1152
894
534
3563
6126
10856
15545
UNT
DTX
C
UNT
DTX
D
delta elongation (treated-baseline)
baseline elongation
HCI-010
PIM001-P
WHIM-14
BCM-15116
BCM-2147
R²=0.75
P=0.0570

Figure 7

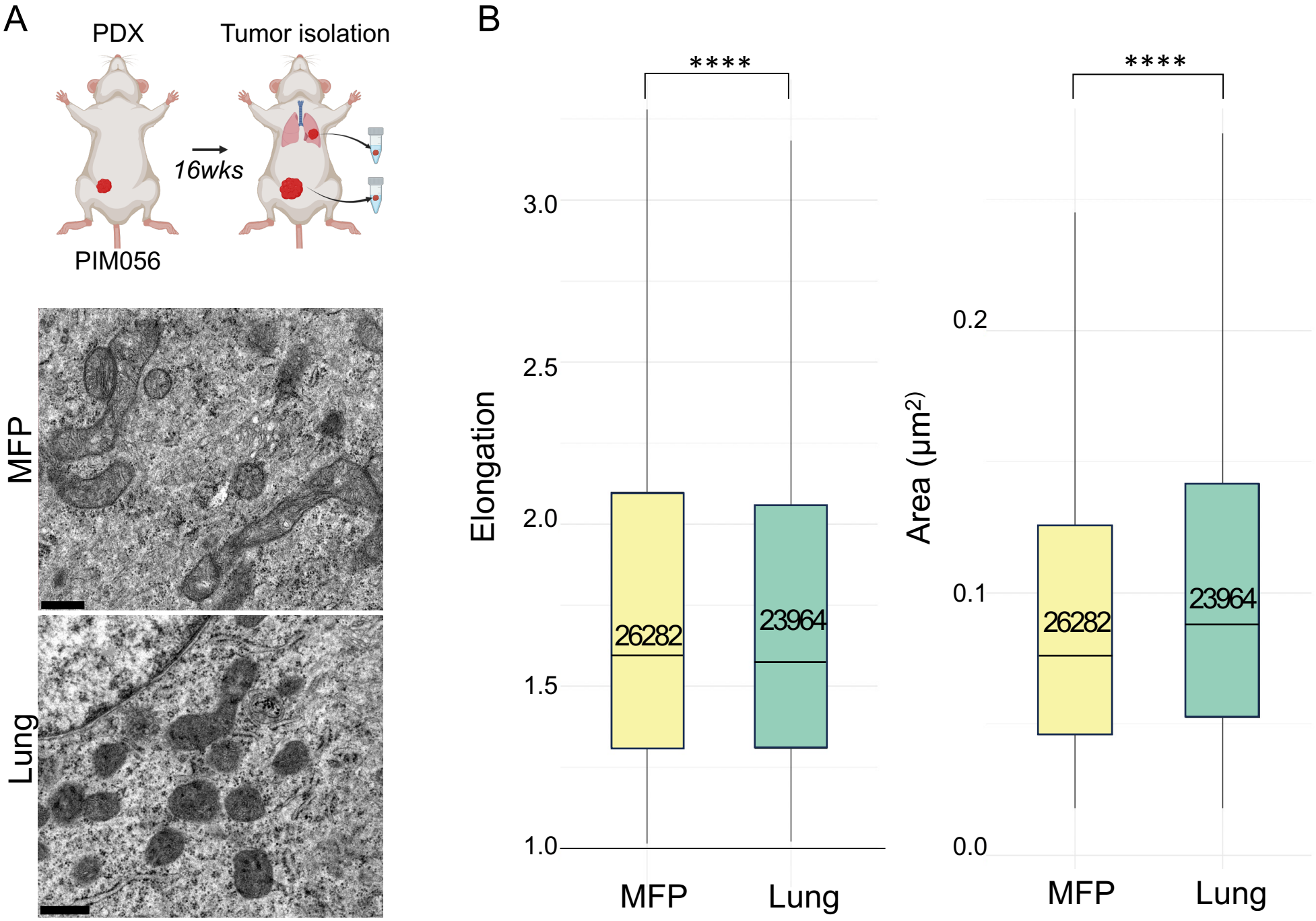
A
PDX
Tumor isolation
16wks
PIM056
MFP
Lung
B
****
****
Elongation
3.0
2.5
2.0
1.5
1.0
26282
23964
MFP
Lung
Area (µm²)
0.2
0.1
0.0
26282
23964
MFP
Lung

Table 2

Sample type	Model name	Cell type	Condition	Tumor location	Min_caliper (μm)	SD	Max_caliper (μm)	SD
In vitro	*Drp1* KO	Mouse myotube	Wild-type	-	0.268	0.11	0.561	0.37
			Drp1 KO	-	0.268	0.14	0.742	0.65
	MDA-MB-231	Human TNBC	Control	-	0.302	0.15	0.623	0.44
			DTX	-	0.289	0.12	0.543	0.35
			DXR	-	0.296	0.12	0.641	0.41
			CRB	-	0.312	0.14	0.675	0.44
			PTX	-	0.242	0.08	0.489	0.28
In vivo	BCM15116	Human TNBC	Untreated	primary	0.248	0.12	0.489	0.31
			DTX	primary	0.256	0.14	0.478	0.25
	BCM2147	Human TNBC	Untreated	primary	0.282	0.12	0.576	0.36
			DTX	primary	0.285	0.13	0.541	0.34
	HCI-010	Human TNBC	Untreated	primary	0.251	0.08	0.445	0.25
			DTX	primary	0.265	0.09	0.470	0.26
	WHIM-14	Human TNBC	Untreated	primary	0.305	0.11	0.592	0.32
			DTX	primary	0.261	0.11	0.479	0.25
	PIM001-P	Human TNBC	Untreated	primary	0.231	0.08	0.447	0.29
			DTX	primary	0.183	0.07	0.346	0.17
	PIM005	Human TNBC	Untreated	primary				
	PIM056	Human TNBC	-	primary	0.286	0.11	0.545	0.34
			-	lung	0.259	0.09	0.505	0.31
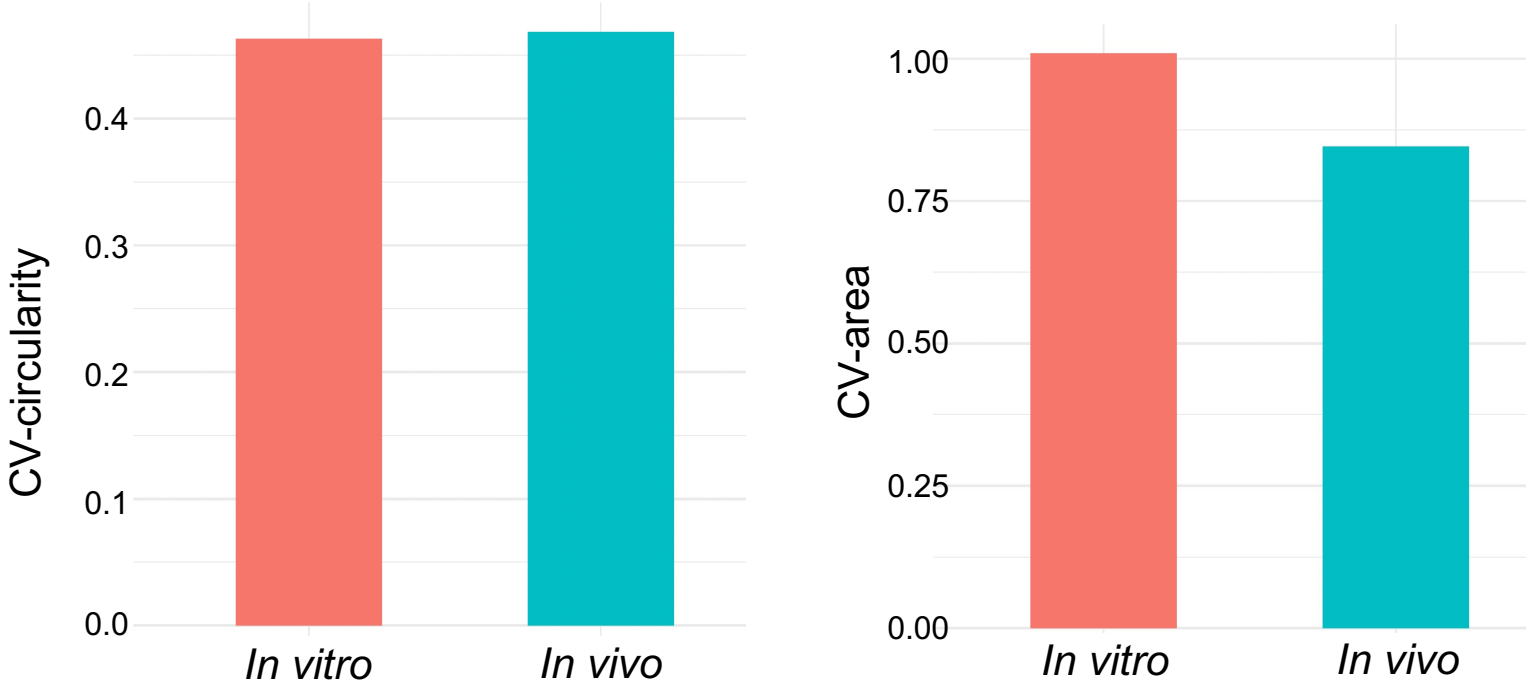
Supplementary Figure 1